

Simultaneous *Swift* and REM monitoring of the blazar PKS 0537–441 in 2005

E. Pian¹, P. Romano^{2,3}, A. Treves⁴, G. Ghisellini², S. Covino², A. Cucchiara⁵, A. Dolcini⁴, G. Tagliaferri², C. Markwardt⁶, S. Campana², G. Chincarini^{2,3}, N. Gehrels⁶, P. Giommi⁷, L. Maraschi⁸, S.D. Vergani^{9,10}, F.M. Zerbi², E. Molinari², V. Testa¹¹, G. Tosti¹², F. Vitali¹¹, L.A. Antonelli¹¹, P. Conconi², G. Malaspina², L. Nicastro¹³, E. Palazzi¹³, E.J.A. Meurs⁹, L. Norci¹⁰

ABSTRACT

The blazar PKS 0537–441 has been observed with all instruments of the *Swift* satellite between the end of 2004 and November 2005. The BAT monitored it recurrently for a total of 2.7 Ms, and the XRT and UVOT pointed it on seven occasions for a total of 67 ks, making it one of the AGNs best monitored by *Swift*. The automatic optical and near-infrared telescope REM has monitored simultaneously the source at all times. In January–February 2005 PKS 0537–441 has been detected at its brightest in optical and X-rays: more than a factor of 2 brighter in X-rays and about a factor 60 brighter in the optical than observed in December 2004. The July 2005 observation recorded a fainter X-ray state, albeit still brighter than the historical average. The simultaneous optical state, monitored by both *Swift* UVOT and REM, is high, and in the VRI bands it is comparable to what was recorded in early January 2005, before the outburst. In November 2005, the source subsided both in X-rays and optical to a quiescent state, having decreased by factors of ~ 4 and ~ 60 with respect to the January–February 2005 outburst, respectively. Our monitoring shows an overall well correlated optical and X-ray decay, with no measurable time lag larger than about 1 month. On the shorter time scales (days or hours), there is no obvious correlation between X-ray and optical variations, but the former tend to be more pronounced, opposite to what is observed on monthly time scales. The widely different amplitude of the long term variability in optical and X-rays is very unusual and makes this observation a unique case study for blazar activity. The spectral energy distributions are interpreted in terms of the synchrotron and inverse Compton mechanisms within a jet where the plasma radiates via internal shocks and the dissipation depends on the distance of the emitting region from the central engine.

Subject headings: BL Lacertae objects: individual (PKS 0537-441) — galaxies: active — gamma-rays: observations — radiation mechanisms: non-thermal

¹INAF - Trieste Astronomical Observatory, Via G.B. Tiepolo, 11, 34143 Trieste, Italy

²INAF - Brera Astronomical Observatory, Via E. Bianchi, 46, 23807 Merate (LC), Italy

³Department of Physics, University of Milano-Bicocca, Piazza delle Scienze, 3, 20126 Milan, Italy

⁴Department of Physics and Mathematics, University of Insubria, Via Valleggio, 11, 22100 Como, Italy

⁵Department of Astronomy and Astrophysics, Pennsylvania State University, University Park, PA 16802, USA

⁶NASA Goddard Space Flight Center, Code 661, Greenbelt, MD 20771, USA

⁷ASI Science Data Center, ASDC c/o ESRIN, Via G. Galilei,

00044 Frascati, Italy

⁸INAF - Brera Astronomical Observatory, Via Brera, 28, 20121 Milano, Italy

⁹Dunsink Observatory - DIAS, Dunsink Lane, Dublin 15, Ireland

¹⁰School of Physical Sciences and NCPST, Dublin City University - Dublin 9, Ireland

¹¹INAF - Rome Astronomical Observatory, Via di Frascati, 33, 00040 Monte Porzio Catone, Italy

¹²Department of Physics, University of Perugia, Via A. Pascoli, Perugia, Italy

¹³INAF - Institute of Space Astronomy and Cosmic Physics, Via Gobetti, 101, 40129 Bologna, Italy

1. Introduction

Multiwavelength variability is the most effective diagnostic tool of the properties of extragalactic jets and of their central engines. Due to the orientation of their jets - nearly aligned to our line of sight - blazars allow a better insight into their inner regions than other radio loud Active Galactic Nuclei (AGN) do, because the intrinsic flux variability is magnified by relativistic effects. Past observations of blazars have identified the active emission mechanisms (synchrotron process at frequencies up to the soft, and occasionally hard, X-rays and inverse Compton scattering at higher energies, Ulrich, Maraschi & Urry 1997; Pian et al. 1998; Tagliaferri et al. 2003; Krawczynski et al. 2004; Dermer & Atoyan 2004; Błażejowski et al. 2005; Sokolov & Marscher 2005; Aharonian et al. 2006; Albert et al. 2006; Kato, Kusunose & Takahara 2006; Massaro et al. 2006; Raiteri et al. 2006). Yet, the structure of the jet, the mechanisms of the energy transfer from the central engine to the emitting particles, and the dissipation processes along the jet are not clear. Intensive monitorings and good coverage at all frequencies are necessary to explore the multiwavelength variability of blazars to its full extent and to understand how the jet interacts with other circumnuclear components to produce the radiation. The *Swift* satellite (Gehrels et al. 2004), with its easy and flexible scheduling, can be optimally employed for the observation of bright blazars (Giommi et al. 2006; Sambruna et al. 2006; Tramacere et al. 2006).

The blazar PKS 0537–441 ($z = 0.896$) is a bright emitter at all frequencies from radio to gamma-rays. In the latter band it has been observed many times by EGRET and detected in different states (Treves et al. 1993; Hartman et al. 1999; Pian et al. 2002). The source was targeted for long term optical and NIR monitoring with the automatic optical/near-IR 60cm telescope Rapid Eye Mount (REM, Zerbi et al. 2001; Chincarini et al. 2003; Covino et al. 2004) in December 2004 - March 2005, when the blazar exhibited a flare with a time scale of about a month (Dolcini et al. 2005). At that time, *Swift* had observed PKS 0537–441 for calibration purposes. On 25 June 2005, the *RXTE* All Sky Monitor recorded a high X-ray (2–10 keV) state of the source, with a flux of (13 ± 5) milli-Crab. The REM monitoring in the optical also revealed the blazar to be active (Covino et al. 2005). Based on these alerts, we requested observations of PKS 0537–441 as a Target of Opportunity with *Swift*. A first ob-

servation was scheduled in July 2005. A second *Swift* visit took place in November 2005, in order to monitor the long-term behavior of the source after the June 2005 outburst. We report here the results of all *Swift* observations of PKS 0537–441, and of the simultaneous REM observations in July and November 2005.

2. Data acquisition, reduction and analysis

2.1. X-ray observations

2.1.1. *Swift*/BAT

PKS 0537–441 was often in the field of view of the *Swift* Burst Alert Telescope (BAT, 15–150 keV) from December 2004 to November 2005. The BAT data were analysed using the standard BAT analysis software distributed within FTOOLS v6.0.5. Although the blazar is not detected in individual *Swift* orbits by BAT, averaging the BAT signal during all periods of observation results in significant flux detection. A spectrum of the integrated data set was extracted and fitted to a single power-law $F_\nu \propto \nu^{-\beta}$ with spectral index $\beta = 0.5 \pm 0.5$ (reduced $\chi^2 = 1.03$). The flux in the 15–150 keV band is $(3.2^{+0.9}_{-2.3}) \times 10^{-11}$ erg cm⁻² s⁻¹.

2.1.2. *Swift*/XRT

The blazar was observed with the X-Ray Telescope (XRT, 0.2–10 keV, Burrows et al. 2005) in December 2004–February 2005, July 2005, and November 2005. The monitoring is organized in seven observations, four of which were obtained during the *Swift* XRT calibration phase. The XRT data were first processed by the *Swift* Data Center at NASA/GSFC into Level 1 products (calibrated and quality-flagged event lists). Then they were further processed with the latest Heasoft release¹ (v6.0.5) to produce the final cleaned event lists. In particular, we ran the task `xrtpipeline` (v0.10.3) applying standard filtering and screening criteria, i.e., we cut out temporal intervals during which the CCD temperature was higher than -47 °C, and we removed hot and flickering pixels which are present because the CCD is operating at a temperature higher than the design temperature of -100 °C due to a failure in the active cooling system. An on-board event threshold of ~ 0.2 keV was also applied to the central pixel, which has been proven to reduce most of the background due to either the bright Earth limb or the

¹<http://swift.gsfc.nasa.gov/docs/software/lheasoft>

CCD dark current (which depends on the CCD temperature). Given the low rate of PKS 0537–441 during the observing campaign (< 0.5 counts s^{-1} in the 0.2–10 keV range), we only considered photon counting data for our analysis (PC; see Hill et al. 2004 for a full description of read-out modes) and further selected XRT grades 0–12, (according to *Swift* nomenclature; Burrows et al. 2005). A summary of the XRT observations is reported in Table 1.

PKS 0537–441 was detected in the XRT data at the coordinates RA(J2000)= $05^h38^m50^s.38$, Dec(J2000)= $-44^\circ05'09''.1$, with an estimated uncertainty of $3''.5$ arcseconds radius (90% containment). This position takes into account the correction for the misalignment between the telescope and the satellite optical axis (Moretti et al. 2006), and is consistent with the source catalog position (ICRS coordinates are RA(J2000)= $05^h38^m50^s.36$, Dec(J2000)= $-44^\circ05'08''.94$).

We extracted the source events in a circle with a radius of 30 pixels ($\sim 71''$), which corresponds to $\sim 94\%$ of the XRT PSF. To account for the background, the data were also extracted within an annular region (radii 55 and 95 pixels) centered on the source and devoid of background sources.

The source and background spectra were extracted in the regions described above. Ancillary response files were generated with the task `xrtmkarf`, and account for differences in extraction regions and PSF corrections. We used the latest spectral redistribution matrices (RMF, v008). The adopted energy range for spectral fitting is 0.3–10 keV, and all data were rebinned with a minimum of 20 counts per energy bin to allow χ^2 fitting within XSPEC (v11.3.2). The only exception was the observation of 23 December 2004, when the number of counts was limited (~ 140) and Cash (1979) statistics was appropriate, therefore ungrouped data were used instead.

The spectra do not exhibit significant features, either in absorption or emission, superimposed on the power-law continuum (see a representative spectrum in Figure 1). We considered an absorbed power-law model, with the neutral hydrogen column kept fixed to its Galactic value (2.91×10^{20} cm^{-2} , Murphy et al. 1996), and the spectral index left as a free parameter. The fit results are reported in Table 1.

2.2. Optical observations

The *Swift* UltraViolet-Optical Telescope (UVOT, Roming et al. 2005) observed PKS 0537–441 in July

(only U,B and V filters) and November 2005 (all filters) simultaneously with the XRT. The log of the observations is reported in Table 2. UVOT data were taken also in December 2004 and January 2005, but due to early orbit checkout and calibration, they are not reliable, and therefore we have not used them. The data analysis was performed using the “uvotsource” task included in the latest *Heasoft* software (see Section 2.1.2). We subtracted the background, and corrected for the coincidence loss effect (similar to the pileup for the XRT) in the case of a bright source. The magnitudes were converted into fluxes using the latest in-flight flux calibration factors and zero-points.

REM acquired photometry of the AGN from December 2004 to March 2005, and also in July and in November 2005, with various combinations of filters. The data reduction followed standard procedures (see Dolcini et al. 2005). The log of the July and November 2005 observations is reported in Table 2, while the details of the previous REM observations have been presented in Dolcini et al. (2005).

3. Results

3.1. Multiwavelength light curves

With a total *Swift*/XRT exposure of 67 ks, PKS 0537–441 is one of the blazars best monitored by this instrument. Figure 2 shows the observed (i.e., not corrected for Galactic absorption), background-subtracted light curves extracted in the 0.2–1 keV and 1–10 keV energy bands. For direct comparison with the X-rays, the merged UVOT and REM light curve in the V band (covered by both instruments) is also shown in Figure 2. The UVOT V-band fluxes have been reduced to the central wavelength of the REM V-band observations using the power-law $F_\nu \propto \nu^{-\beta}$ which best fits the optical spectrum in July ($\beta = 1.84 \pm 0.04$) and November 2005 ($\beta = 1.26 \pm 0.05$). The full transformation equation is $F_{UVOT,5505\text{\AA}} = (5505/5460)^\beta \times F_{0,UVOT-V} \times 10^{-0.4V_{UVOT}}$, where $F_{0,UVOT-V}$ is the flux corresponding to zero UVOT V magnitude (equal to 3.19×10^{-9} and 3.17×10^{-9} erg s^{-1} cm^{-2} \AA^{-1} for the July and November 2005 measurements, respectively). The REM and UVOT V-band data taken closest in time (12 July 2005) differ by $\sim 13\%$, the REM flux being lower than the UVOT flux. This difference may be intrinsic, since the REM and UVOT observations are about 6–7 hours apart, however, it is within the sum of the statistical uncertainties (see Table 2) and the systematic errors due to flux transformation and calibration of the

two instruments (estimated to be no less than $\sim 5\%$ altogether).

The optical V-band and X-ray light curves are highly correlated, however, the V-band flux varies with much higher amplitude. To the initial factor of 60 optical variation detected with REM between end of December 2004 and early February 2005 – noted and discussed in Dolcini et al. (2005) – corresponds a variation of only a factor ~ 2 of both soft (0.2-1 keV) and hard (1-10 keV) X-ray flux (Fig. 2). Thereafter, the flux decays nearly monotonically up to November 2005 both in optical and X-rays, with overall amplitudes of factors of ~ 60 and ~ 4 , respectively. The variability indices of the X-ray light curves, defined as the ratios between the flux standard deviation around the mean flux and the mean flux itself ($\sigma / \langle f \rangle$), are 0.375 and 0.423 for the hard and soft X-rays, respectively, consistently lower than the optical variability index, 1.434 (the variability indices have been computed from the original datasets, i.e. before applying the temporal binning adopted in Figure 2). The time behavior of the hardness ratio between the bands 0.2-1 keV and 1-10 keV shows no clear long term trend: the spectrum hardens up to summer 2005 and softens thereafter, but only with marginal significance (Fig. 3a).

In Figure 4 portions of the light curves are reported in smaller time intervals. The X-ray flux presents an almost fully resolved flare on 27-28 January 2005 with somewhat higher total amplitude in the soft than in the hard band (factors of ~ 2 and ~ 1.5 , respectively, see Fig. 3b and Fig. 4a). The correlated optical and X-ray behavior on short time scales (days to hours) has no precise character: while the limited simultaneous X-ray and optical sampling in July 2005 shows a well correlated decay in the 2 bands, with the X-ray flux declining faster than the optical flux (Fig. 4b), the factor of 2 X-ray variations in November 2005 have no counterpart in UV-optical, where flickering of at most $\sim 10\%$ is observed (Fig. 4c,d).

Obviously, the better long term sampling available at optical wavelengths favours the detection of day time scale variations in optical with respect to the X-rays. This is relevant when attempting to determine a possible time lag between the optical and X-ray light curves. While we can constrain the occurrence of the optical maximum (formally observed on 5 February 2005) within the time window 3-12 February 2005, the X-ray light curve maximum is much less well constrained. Fig. 4a indicates that the X-ray observed

maximum occurred between 27 and 28 January 2005. If this is the absolute peak of the X-ray light curve, and it is correlated with that in the optical, then it has preceded the optical maximum by at least one week in the observer frame. However, given the sampling of the X-ray light curve, we cannot exclude more intense and unobserved flares preceding or following the observed X-ray maximum by time intervals of up to ~ 1 month. Therefore, this is our upper limit on the time lag of the correlation between the X-ray and optical light curves.

3.2. Broad-band spectrum

In Figure 5 we report the broad-band spectral energy distributions of PKS 0537–441 at three epochs during our *Swift* and REM campaign, representative of three different emission states: 24-25 February, 12 July and 24 November 2005 for the bright, intermediate and low state, respectively. The spectral energy distribution of 24 November 2005 has been selected because the *Swift*/UVOT observations made on that day cover the near-UV wavelengths (1930-2600 Å), unlike those of 17 November, that are limited to the UBV filters (Table 2). However, no strictly simultaneous REM data are available on 24 November. The REM data of 20 and 30 November 2005 have been used instead, and interpolated at the date of 24 November. We exclude that possible variability between 20 and 30 November 2005 may significantly affect the reliability of the REM fluxes obtained through interpolation: no large variability is observed in this period (see Table 2); the UVOT and REM V-band points are consistent (see Fig. 5); we have verified that the shape of the near-IR-to-near-UV spectrum of 24 November 2005 is similar to that of 17 November 2005 (constructed with data simultaneous within 1 day), in the common wavelength range (3400–16000 Å).

Whenever more than one UVOT or REM measurement is available at a given date and filter, we take the flux average. The associated error is the standard deviation when three or more data points are averaged. When only two measurements are available, the error is the larger of the two individual errors, or the flux difference, whichever is larger. The X-ray data are corrected for photoelectric absorption by the Galactic neutral hydrogen as described in Section 2.1.2, and the near-infrared to ultraviolet data are corrected for Galactic dust absorption with $E(B - V) = 0.037$ (Schlegel, Finkbeiner, & Davis 1998), using the extinction law of Cardelli, Clayton, & Mathis (1989). For comparison, we have reported also the historical

multiwavelength spectra obtained in 1991-1992 and 1995 (see Pian et al. 2002) and the non-simultaneous IRAS, ISO, HST and BeppoSAX data taken at various epochs (Padovani et al. 2006; Pian et al. 2002).

The 2005 optical spectra, spanning a factor of ~ 50 in normalization, bracket the historical optical observations. They are described by single power-laws and are steeper at higher states. The near-IR flux varies with lower amplitude. At the lowest state of November 2005, we note a large discrepancy between the optical and infrared fluxes: the H-band flux exceeds by a factor of ~ 4 the extrapolation of the optical spectrum to the H-band wavelengths. The flatness of the November optical-UV spectrum and the spectral discontinuity between the optical and near-IR wavebands suggest that in the lower states different emission components play a role in shaping the spectrum. In particular, radiation produced by the accretion disk may partially account for the optical-UV spectrum. This behavior is reminiscent of that seen in 3C 279 (Pian et al. 1999).

The X-ray fluxes detected by XRT encompass both the BeppoSAX and ROSAT states. The steadiness of the XRT spectral slope over time, as opposed to a factor 4 variation in the normalization, is remarkable. The X-ray spectral shape is also very similar to that of the BeppoSAX spectrum, which covers an energy range similar to that covered by XRT.

The BAT spectrum is dominated by the episodes of more intense activity of January-February and July 2005, and despite its large uncertainty gives a good estimate of the spectral shape at hard X-rays in high state.

4. Discussion

The character of the multiwavelength variability detected by our monitoring is extremely unusual: the outburst of PKS 0537-441, jointly monitored by XRT and REM from its rise in December 2004 - January 2005 to its long decay ended in November 2005, has a remarkably higher amplitude at optical (factor of ~ 60) than at X-ray frequencies (factor of ~ 4). These obviously represent only lower limits to the variability, the intrinsic amplitude of which may be contaminated by a constant component that is more relevant in X-rays than in the optical. The optical spectra suggest the presence of an underlying thermal optical component in low state (Section 3.2), presumably only modestly variable. However, trying to assess whether - and how significantly - this dilutes the intrinsic multiwave-

length variability of the non-thermal flux is prone to many uncertainties. The sampling of our monitoring indicates that the long-term decay is monotonic (Fig. 2), but small flares are present on day time scales (Fig. 4).

The fact that the optical-UV flux variability has a much larger amplitude than the simultaneous X-ray flux variability, may at first sight be surprising. In a simple synchrotron self-Compton scenario, where the optical emission is due to synchrotron radiation and the X-rays are due to inverse Compton scattering off the synchrotron photons, one would expect to observe the opposite if the changing parameter is the density of the emitting particles. In fact, the self-Compton emissivity scales with the square of the particle density, while the synchrotron emissivity varies linearly with it. If instead the varying parameter is the magnetic field, we expect that both the synchrotron and the synchrotron self-Compton fluxes vary with the same amplitude.

On the other hand, in models producing the high energy emission by upscattering of radiation produced outside the jet ("external" Compton) both the synchrotron and the inverse Compton fluxes vary linearly with the particle density. In these models, a variation of the magnetic field could produce a variation of the synchrotron flux leaving almost unchanged the inverse Compton flux.

Note also that the X-ray and optical spectra in these models derive from very different portions of the relativistic electron distribution: the optical emission originates from electrons above the spectral break, while the X-rays are produced via inverse Compton scattering of synchrotron or external photons by electrons of much lower energies.

We applied a simple, one-zone, homogeneous synchrotron self-Compton plus external inverse Compton model to the different states of PKS 0537-441. The model is described in Ghisellini, Celotti & Costamante (2002). The general assumptions are the following:

- The source is a cylinder of cross sectional radius $R = \psi z$, where z is the distance from the apex of the jet, assumed to be a cone of semi-aperture angle ψ . The width $\Delta R'$, as measured in the co-moving frame, is assumed to be equal to R ;
- the magnetic field B is homogeneous and tangled;
- the blob moves with a bulk Lorentz factor Γ and

the viewing angle is θ (we assumed here $\theta = 3^\circ$);

- the external radiation is produced at a fixed radius, which can be identified with the radius of the broad line region. We assume that 10% of the disk luminosity is reprocessed by the broad line region. These assumptions should be taken with care, because, beside the contribution of the broad line region, other processes can contribute to the external radiation (scattering by ionized intercloud plasma, synchrotron radiation “mirrored” by the clouds and/or the walls of the jet, reprocessing by a molecular torus; Sikora, Begelman, & Rees 1994; Błażejowski et al. 2000; Ghisellini & Madau 1996; and finally, direct radiation from the accretion disk, Dermer & Schlickeiser 1993; see also Celotti, Ghisellini & Fabian 2007);
- the particle distribution is the result of injection and cooling. We calculate the random Lorentz factor γ_{cool} at which the particles cool in one light crossing time. If the particles are injected between γ_{inj} and γ_{max} with a power law distribution of slope s , in the “fast cooling” regime ($\gamma_{\text{cool}} < \gamma_{\text{inj}}$), we have an emitting particle distribution $N(\gamma) \propto \gamma^{-p}$ between γ_{inj} and γ_{max} (where $p = s + 1$ is the injection slope increased by one unit), and $N(\gamma) \propto \gamma^{-2}$ between γ_{cool} and γ_{inj} (Ghisellini et al. 2002; Ghisellini et al. 1998; Ghisellini 1989). In the models presented here, this is always the case, since the adopted parameters (see Table 3) imply that the radiative cooling (synchrotron, synchrotron self-Compton and external Compton) is fast, and guarantee that γ_{cool} is always smaller than γ_{inj} and close to unity (after a light crossing time).

Based on the above assumptions, the modelling of the spectral energy distribution yields the results shown in Fig. 5, where we report model curves for three states of the source during our 2005 campaign. We have also modeled under similar assumptions previous multiwavelength energy distributions of PKS 0537–441, presented in Pian et al. (2002), including data in the MeV–GeV domain from CGRO-EGRET (Fig. 6). The radiation processes at work are synchrotron at radio-to-UV frequencies, and inverse Compton scattering off both synchrotron photons (self-Compton) and external photons, dominating at X-ray and gamma-ray frequencies, respectively.

The input parameters used for these models are listed in the upper part of Table 3. In the lower part we report some interesting output parameters, namely the Doppler factor δ and the power carried by the jet in the form of magnetic field (L_B), cold protons (L_p), relativistic electrons (L_e), and produced radiation (L_{rad}), defined as:

$$\begin{aligned} L_B &= \pi R^2 \Gamma^2 c U_B \\ L_p &= \pi R^2 \Gamma^2 c \int N(\gamma) m_p c^2 d\gamma \\ L_e &= \pi R^2 \Gamma^2 c \int N(\gamma) \gamma m_e c^2 d\gamma \\ L_{\text{rad}} &= \pi R^2 \Gamma^2 c U'_{\text{rad}} \end{aligned} \quad (1)$$

where U_B and U'_{rad} are the magnetic and the radiation energy density measured in the comoving frame, respectively.

Usually, when applying a single-zone synchrotron and inverse Compton model, the choice of the input parameters is not unique, especially when the peak of the inverse Compton component is not observed, as in our case. However, we were guided in our choice by the knowledge of the total luminosity of the broad lines ($\sim 5 \times 10^{44} \text{ erg s}^{-1}$, Pian, Falomo, & Treves 2005), and the requirement that the spectra observed here in the low optical–UV state are unusually flat because they are “contaminated” by the thermal accretion disk component. We can then infer the luminosity of this component (which we have fixed to $1.8 \times 10^{46} \text{ erg s}^{-1}$). Note also that in the low state of November 2005 the flux in the H filter suggests that the synchrotron spectrum on these occasions is very steep. The other requirements we have applied, which help us in choosing the input parameters, include minimizing the total power budget and describing the different states of the source with a minimal change of the power carried by the jet. The latter point is crucial, because it allows a direct test once high energy observations – as will be performed by GLAST – will be available. In fact it is possible to obtain reasonably good fits by allowing the jet power to vary by a large amount from state to state, being larger in high states. This would however correspond to very different spectra and fluxes in the MeV–GeV band.

Remarkably, the chosen parameters correspond closely to the expectations of the jet radiation model proposed by Katarzyński & Ghisellini (2007): dramatic variations in specific frequency bands can be produced by relativistic jets carrying the same amount

of energy in bulk relativistic and Poynting flux form. In fact, if blobs having the same bulk kinetic energy ΓMc^2 (where M is the mass of the blob) dissipate a fraction of their kinetic energy at different locations along the jet, and if the distance of the emitting region from the origin of the jet is directly related to Γ , then slow blobs will dissipate closer to the jet apex, when the blob is more compact, and embedded in a larger magnetic field. In this case the external Compton scattering is reduced because the external radiation energy density as seen in the comoving frame ($\propto \Gamma^2$) is lower, while the synchrotron radiation ($\propto B^2$) is likely to be enhanced, since we expect larger values of the magnetic field closer to the apex of the jet.

In this picture the key ingredient is the link between the dissipation site and the bulk Lorentz factor at that location: smaller Lorentz factors are required for smaller distances between the jet apex and the dissipation site. There are two scenarios: the blob could be still accelerating when it dissipates, or else the dissipation is the result of internal shocks. In Katarzyński & Ghisellini (2007) the second scenario is adopted, because it provides the scalings needed to characterize completely the model. In this scenario (see its specific application to blazars by Ghisellini 1999, Spada et al. 2001; Guetta et al. 2004), faster blobs can catch up with slower ones at a distance $z = \Gamma^2 \Delta z_0$ from the jet origin, where z_0 is the initial separation of the two blobs, and Δ is their thickness.

Furthermore, in the Katarzyński & Ghisellini (2007) model, it is assumed that the blobs always carry the same amount of bulk kinetic energy (ΓMc^2 is the same) and magnetic energy ($\Gamma B^2 V'$ is the same, where B and V' are the magnetic field and volume measured in the comoving frame of the source, respectively). As a result of the dissipation process, the fraction of the available energy transferred to the emitting electrons is the same (i.e., the efficiency is the same). Based on these assumptions, we can assign for all the input parameters their scalings with Γ : therefore, when fitting two or more different states of the same source with this model, once we have chosen the parameters for one state we are left with only one free parameter, i.e. the bulk Lorentz factor Γ . We can relax this by allowing the particle distribution slopes to be changed, as well as the fraction of the electron population which is accelerated to relativistic energies. This does not violate any strong requirement.

In Fig. 7 it is shown how the choice of the present input parameters compares with the Katarzyński &

Ghisellini (2007) prescriptions, namely $B \propto \Gamma^{-7/2}$, $R \propto \Gamma^2$ and $L'_{\text{inj}} \propto \Gamma^{-3}$. We also show (bottom panel) that the power carried by the jet is almost constant. The good agreement leads us to conclude that the variations seen in this source are probably due to (small) variations in the bulk Lorentz factor, which induces dissipation to occur at different locations along the jet. Consequently, the emitting regions have different radii, particle densities and magnetic fields. Note that variations of Γ between 10 and 15 can explain the entire observed variability. In this respect, PKS 0537–441 is very similar to 3C 454.3 during its large 2005 multiwavelength flare (Fuhrmann et al. 2006; Pian et al. 2006; Giommi et al. 2006). For that source, the 100-fold amplitude of the optical variability could be accounted for by changing Γ by a factor of less than 2 (Katarzyński & Ghisellini 2007).

The knowledge of the spectrum of PKS 0537–441 at MeV-GeV energies is crucial for fully constraining the models. Therefore, PKS 0537–441 qualifies as a prime candidate for further monitoring with *Swift* and for simultaneous observations with INTEGRAL, AGILE and GLAST.

We thank P. Roming and S. Holland for assistance with the UVOT data, C. Pagani for help with the *Swift* scheduling, and the whole *Swift* team for their support of the mission. We acknowledge use of the quick-look results provided by the *RXTE* All Sky Monitor team. This research has made use of the Simbad database. This work is supported at OABr by ASI grant I/R/039/04 and at OATs by the contracts ASI INTEGRAL I/R/046/04 and ASI-INAF I/023/05/0.

REFERENCES

- Aharonian, F., et al. 2006, *A&A*, 455, 461
- Albert, J., et al. 2006, *ApJ*, 648, L105
- Bersanelli, M., Bouchet, P., & Falomo, E. 1991, *A&A*, 252, 854
- Błażejowski, M., Sikora, M., Moderski, R., & Madejski, G. M. 2000, *ApJ*, 545, 107
- Błażejowski, M., et al. 2005, *ApJ*, 630, 130
- Burrows, D. N., et al. 2005, *Space Sci. Rev.*, 120, 165
- Cardelli, J. A., Clayton, G. C., & Mathis, J. S. 1989, *ApJ*, 345, 245
- Cash, W. 1979, *ApJ*, 228, 939
- Celotti, A., Ghisellini, G., & Fabian, A.C. 2007, *MNRAS*, in press (astro-ph/0611439)
- Chincarini, G., et al. 2003, *The ESO Messenger*, No.113, p. 40-44
- Covino, S., et al. 2004, *AN*, 325, 543
- Covino, S., et al. 2005, *The Astronomer's Telegram* N. 564
- Dermer, C.D., & Schlickeiser, R. 1993, *ApJ*, 416, 453
- Dermer, C.D., & Atoyan, A. 2004, *ApJ*, 611, L9
- Dolcini, A., et al. 2005, *A&A*, 443, L33
- Fuhrmann, L., et al. 2006, *A&A*, 445, L1
- Fukugita, M., Shimasaku, K., & Ichikawa, T. 1995, *PASP*, 107, 945
- Gehrels, N., et al. 2004, *ApJ*, 611, 1005
- Ghisellini, G. 1989, *MNRAS*, 238, 449
- Ghisellini, G., & Madau, P. 1996, *MNRAS*, 280, 67
- Ghisellini, G. 1998, Celotti, A., Fossati, G. Maraschi, L., & Comastri, A. 1998, *MNRAS*, 301, 451
- Ghisellini, G. 1999, *AN*, 320, 232
- Ghisellini, G., Celotti, A., & Costamante, L. 2002, *A&A*, 386, 833
- Giommi, P., et al. 2006, *A&A*, 456, 911
- Guetta, D., Ghisellini, G., Lazzati, D. & Celotti, A. 2004, *A&A*, 421, 877
- Hartman, R.C., et al. 1999, *ApJS*, 123, 79
- Hill, J. E., et al. 2004, *Proc. SPIE*, 5165, 217
- Katarzyński, K., & Ghisellini, G. 2007, *A&A*, 463, 529
- Kato, T., Kusunose, M., Takahara, F. 2006, *ApJ*, 638, 653
- Krawczynski, H., et al. 2004, *ApJ*, 601, 151
- Massaro, E., Tramacere, A., Perri, M., Giommi, P., & Tosti, G. 2006, *A&A*, 448, 861
- Moretti, A., et al. 2006, *A&A*, 448, L9
- Murphy, E.M., Lockman, F.J., Laor, A., & Elvis, M. 1996, *ApJS*, 105, 369
- Padovani, P., Giommi, P., Ábrahám, P., Csizmadia, S., & Moór, A. 2006, *A&A*, 456, 131
- Pian, E., et al. 1998, *ApJ*, 492, L17
- Pian, E., et al. 1999, *ApJ*, 521, 112
- Pian, E., et al. 2002, *A&A*, 392, 407
- Pian, E., Falomo, R., & Treves, A. 2005, *MNRAS*, 361, 919
- Pian, E., et al. 2006, *A&A*, 449, L21
- Raiteri, C.M., et al. 2006, *A&A*, 459, 731
- Roming, P. W. A., et al. 2005, *Space Sci. Rev.*, 120, 95
- Sambruna, R.M., et al. 2006, *ApJ*, 646, 23
- Schlegel, D.J., Finkbeiner, D.P., & Davis, M. 1998, *ApJ*, 500, 525
- Sikora, M., Begelman, M.C., & Rees, M.J. 1994, *ApJ*, 421, 153
- Sokolov, A., & Marscher, A.P. 2005, *ApJ*, 629, 52
- Spada, M., Ghisellini, G., Lazzati, D. & Celotti, A. 2001, *MNRAS*, 325, 1559
- Tagliaferri, G., et al. 2003, *A&A*, 400, 477
- Tramacere, A., et al. 2006, *A&A*, in press (astro-ph/0611276)

Treves, A., et al. 1993, ApJ, 406, 447

Ulrich, M.-H., Maraschi, L., & Urry, C.M. 1997,
ARA&A, 35, 445

Zerbi, F.M., et al. 2001, AN, 322, 275

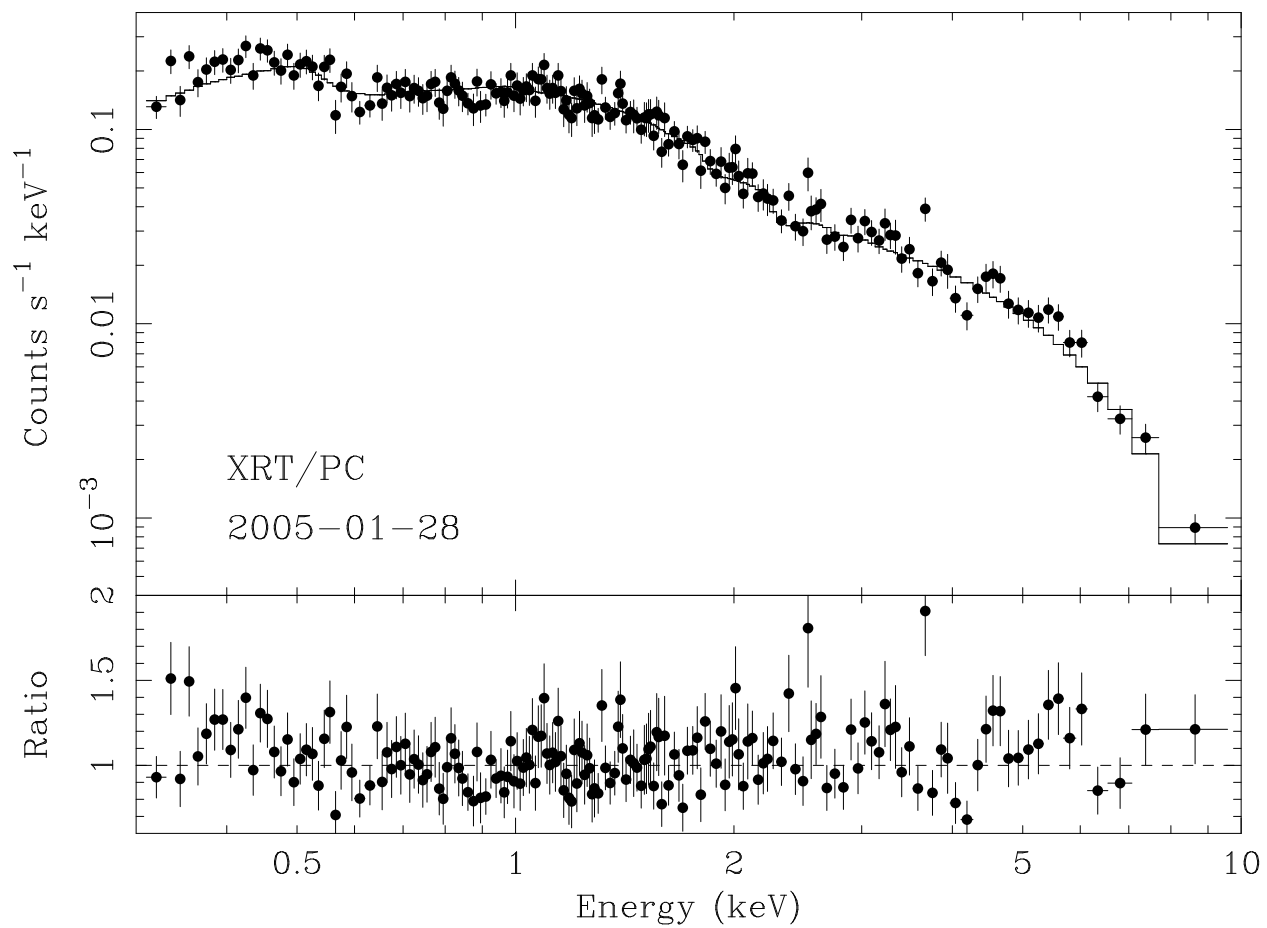


Fig. 1.— Observed *Swift*/XRT spectrum taken on 28 January 2005. The solid stepped curve represents the single absorbed power-law which best fits the spectrum (see Table 1 for spectral parameters).

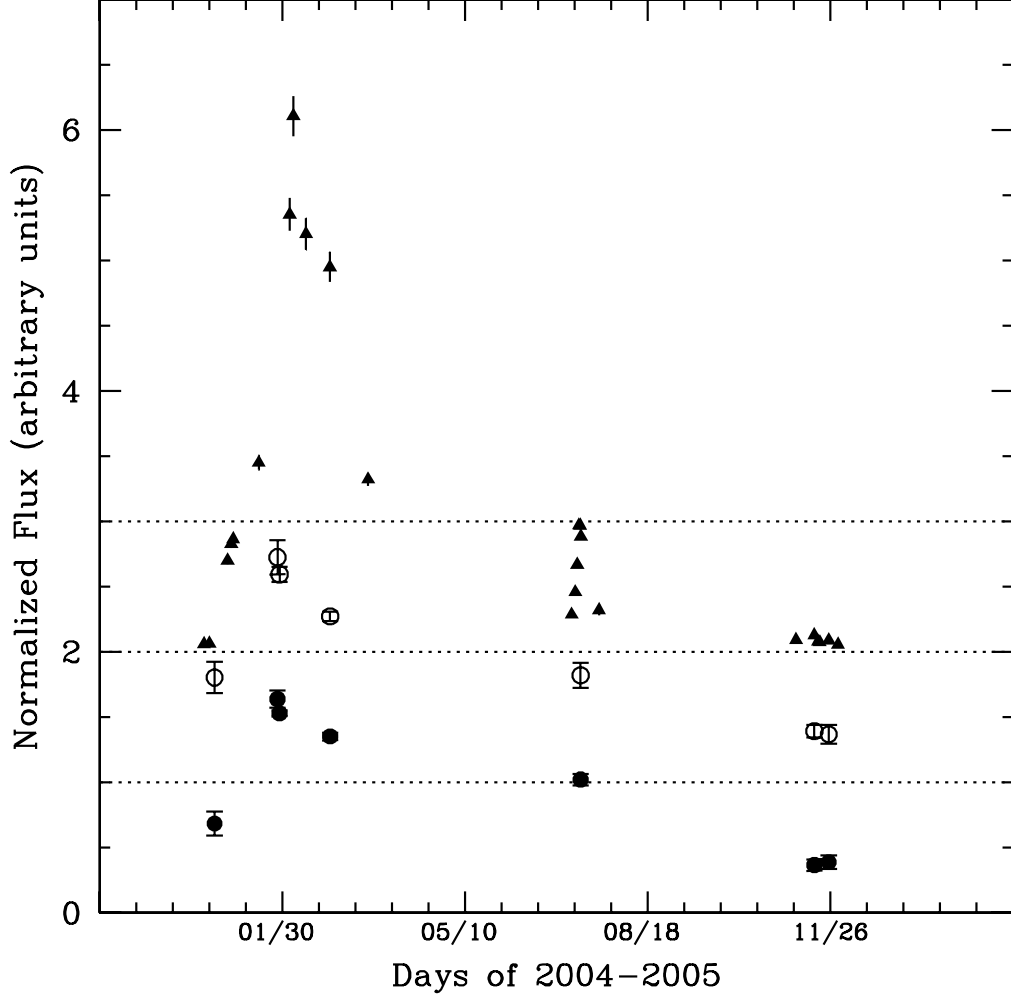


Fig. 2.— *Swift*/XRT background-subtracted light curves in the 1–10 keV (filled circles) and in the 0.2–1 keV (open circles) energy bands, and optical light curve (triangles), obtained from the merging of the UVOT V filter and REM V filter observations. The signal has been averaged within the *Swift* pointings for the X-ray data and with a time resolution of 1 day for the optical data. The curves are not corrected for Galactic extinction, and are normalized to their respective averages (0.136 cts s^{-1} in the 1–10 keV band, 0.084 cts s^{-1} in the 0.2–1 keV band, 6.58 mJy in the optical band), computed on the time-binned datasets. The dotted horizontal lines indicate the average values of the three light curves: for clarity, the 0.2–1 keV band and V-band light curves have been scaled up by additive constants 1 and 2, respectively. Note that this upscaling implies that the flux ratios derived by direct inspection of the soft X-ray (0.2–1 keV) and optical light curves do not correspond to the real ones, the fluxes having been increased by constants 1 and 2, respectively. The maximum amplitudes of variability in optical and X-rays are a factor of ~ 4 and ~ 60 , respectively.

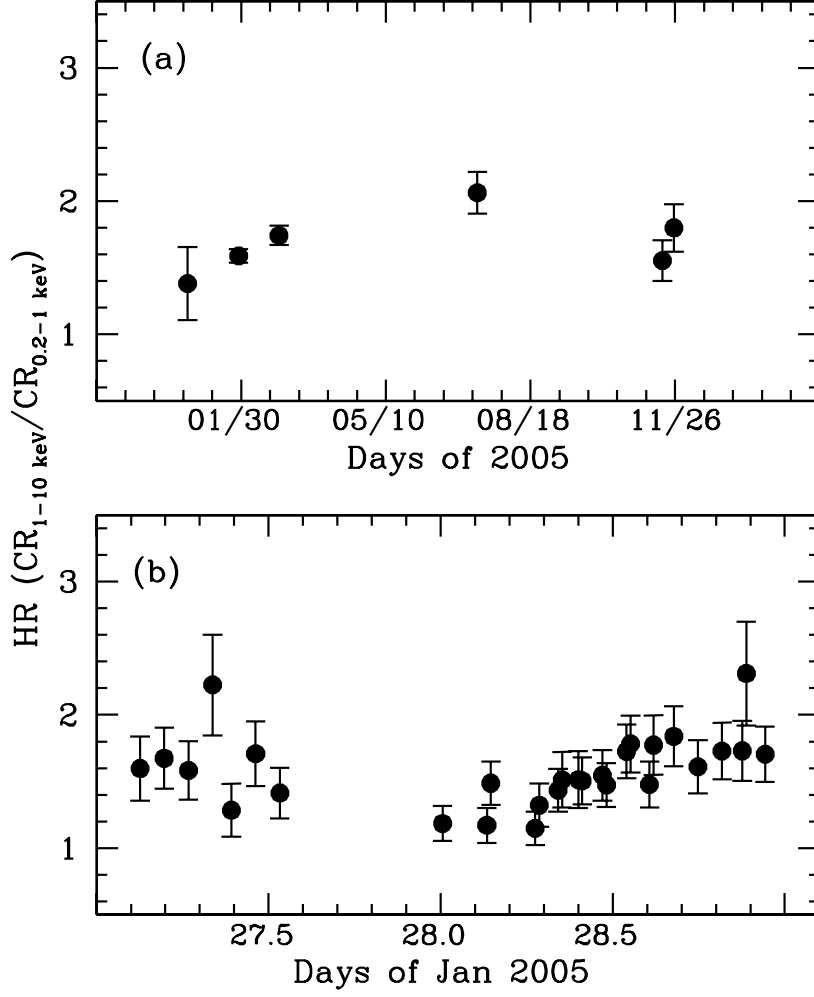


Fig. 3.— Hardness ratios computed using the 1-10 keV and 0.2-1 keV count rates for (a) the whole monitoring; (b) the observation of January 2005.

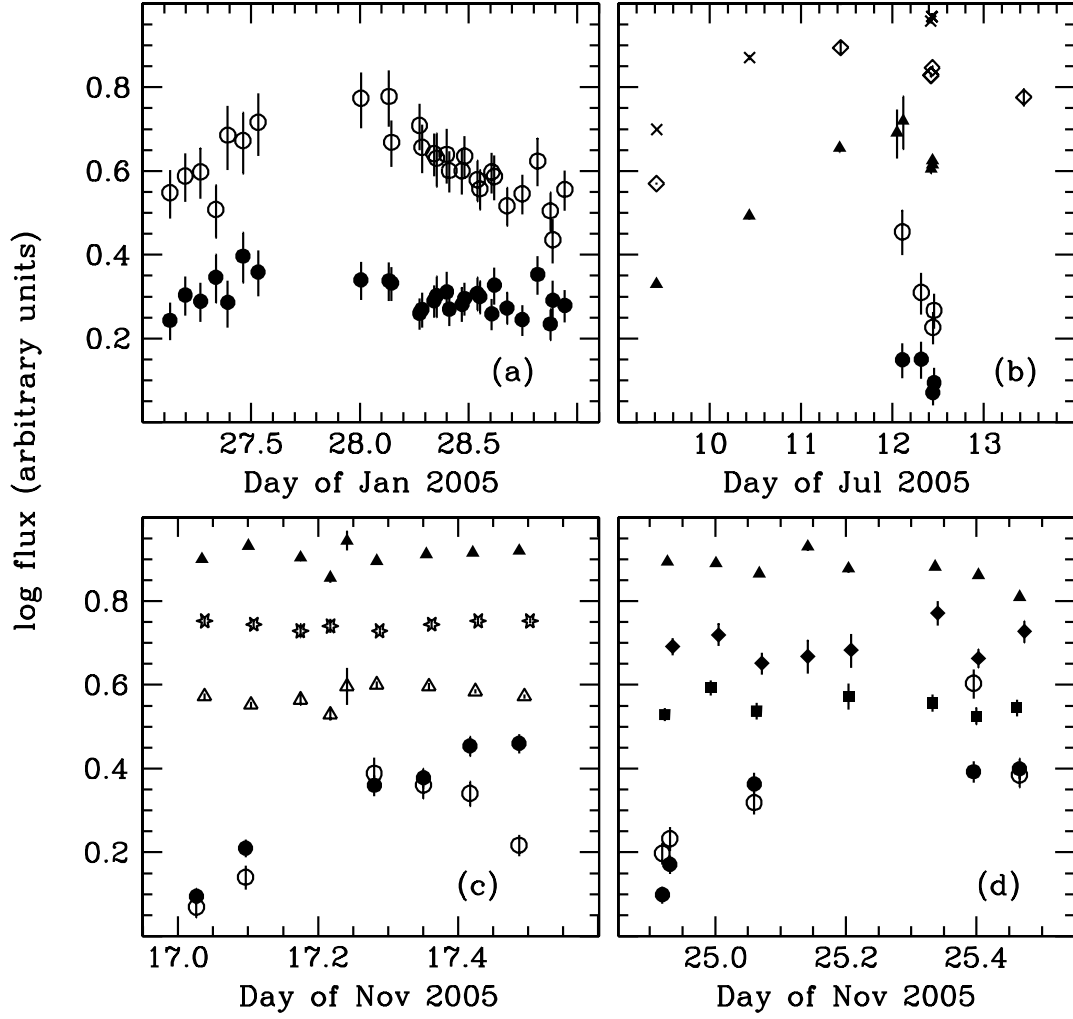


Fig. 4.— Multiwavelength light curves at various epochs during the 2005 campaign, in logarithmic scale, shifted in flux by arbitrary additive constants: (a) 1-10 keV (filled circles) and 0.2-1 keV (open circles) XRT light curves in January 2005; (b) XRT light curves in July 2005 (symbols as in panel (a)), and simultaneous REM and UVOT V-band (filled triangles), REM R- (open diamonds) and I-band (crosses) light curves. Note the optical increase preceding the X-ray observation and the correlated X-ray and optical decay; (c) XRT light curves on 17 November 2005 (symbols as in panel (a)), and UVOT U- (open triangles), B- (stars) and V-band (filled triangles) light curves; (d) XRT light curves in 24-25 November 2005 (symbols as in panel (a)), and UVOT light curves in the W2 (1930 Å, filled squares), W1 (2600 Å, filled diamonds) and V filters (filled triangles).

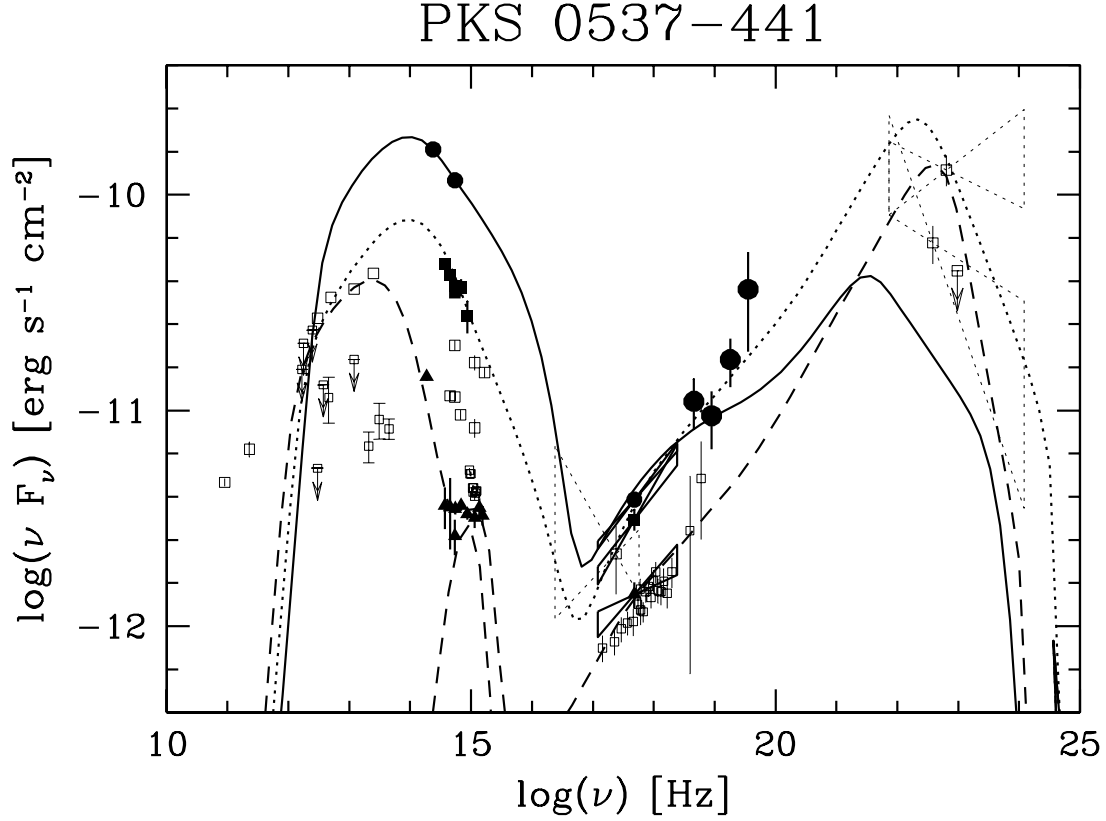


Fig. 5.— Observed spectral energy distributions of PKS 0537-441 on 24-25 February 2005 (small filled circles), 12 July 2005 (filled squares) and 24 November 2005 (filled triangles). The big filled circles represent the BAT data. The *Swift*/XRT data are reported along with the 1σ confidence ranges of their power-law fits. Systematic errors of 5% and 10% have been added in quadrature to the statistical uncertainties associated with the UVOT UVB filters and UV filters data points, respectively. For comparison, in lighter, open squares the multiwavelength data from previous epochs are reported (including CGRO-EGRET spectra), already discussed in Pian et al. (2002), and the non-simultaneous IRAS, ISO, HST-FOS and BeppoSAX data (Pian et al. 2002; Padovani et al. 2006). The 1σ confidence ranges of the EGRET spectra are reported as light dashed lines. The flux uncertainties are 1σ (in some cases they are smaller than the symbol size). The X-ray, UV, optical and near-IR data are corrected for Galactic extinction (see text). The optical and near-IR magnitudes have been converted to fluxes following Fukugita, Shimasaku, & Ichikawa (1995) and Bersanelli, Bouchet, & Falomo (1991), respectively. Overplotted are the jet models (Katarzyński & Ghisellini 2007, see text) for the energy distributions of 24-25 February 2005 (solid curve), 12 July 2005 (dotted curve), 24 November 2005 (dashed curve). The thermal component required to account for the observed optical-UV flux is also reported as a dashed curve.

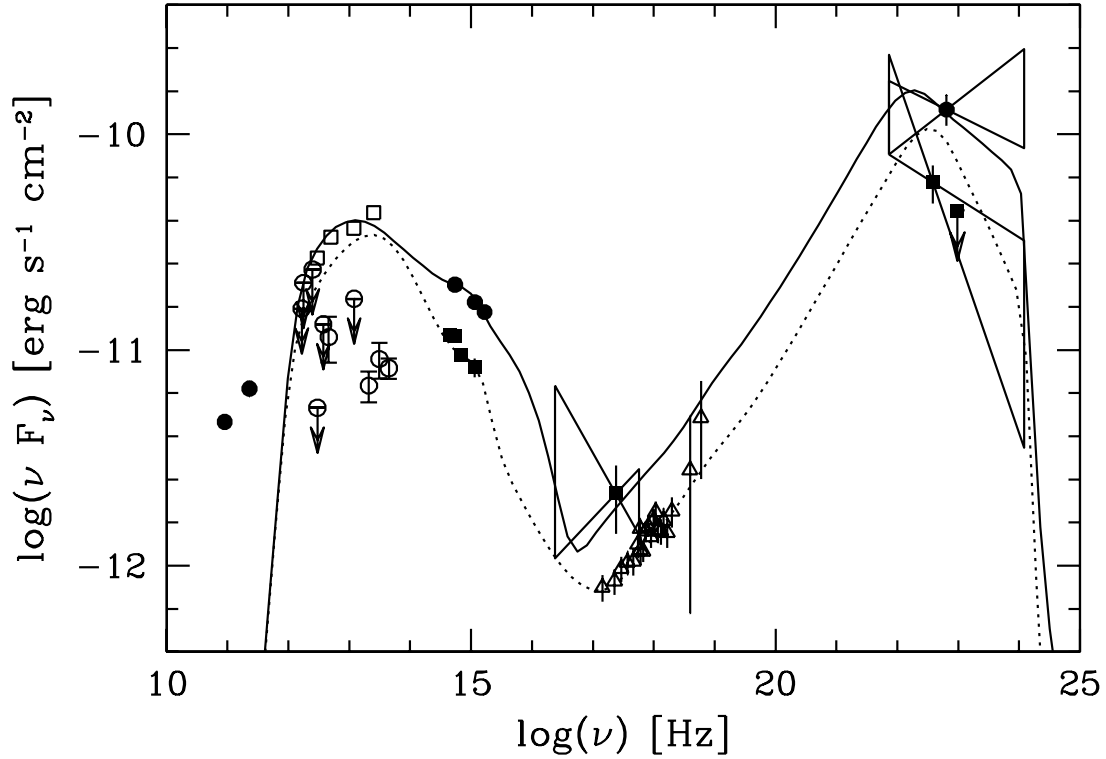


Fig. 6.— Historical spectral energy distributions of PKS 0537–441. The data are the same as those presented in Fig. 5 as open squares. Here we distinguish them according to the observation epoch: the gamma-ray (CGRO-EGRET), soft X-ray (ROSAT), UV (IUE), optical and millimetric data have been taken nearly simultaneously in 1991-1992 (filled squares) and 1995 (filled circles). The far-infrared data taken by IRAS and ISO and the X-ray BeppoSAX data are not simultaneous and are represented as open squares, open circles and open triangles, respectively (see Pian et al. 2002, and references therein; Padovani et al. 2006). As in Fig. 5, the data have been modelled according to Katarzyński & Ghisellini (2007). The model curves for the 1991-1992 and 1995 states are dotted and solid, respectively.

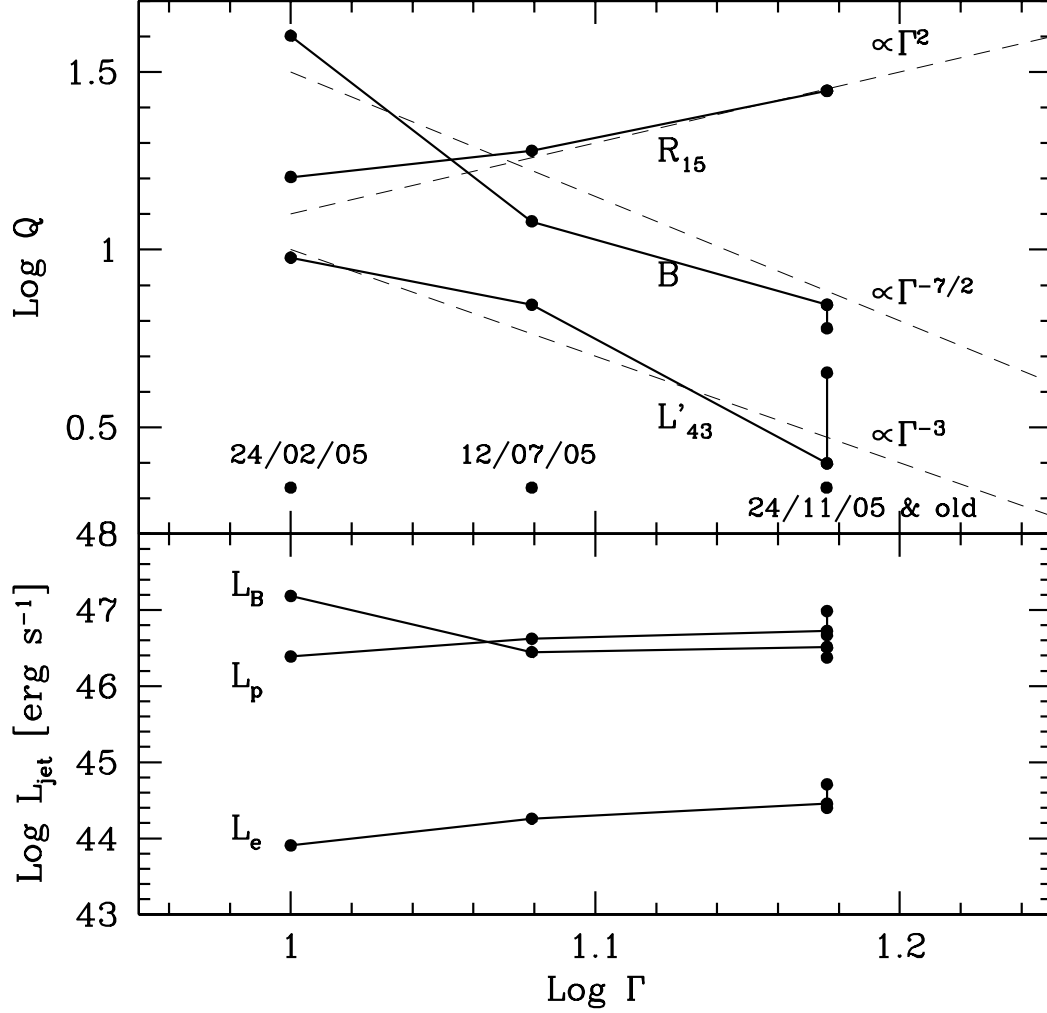


Fig. 7.— *Top panel:* The logarithms of 3 quantities ("Q") are reported as a function of the logarithm of the bulk Lorentz factor: the size of the emitting source R_{15} in units of 10^{15} cm, the value of the magnetic field B in Gauss, and the injected power L'_{43} (in the comoving frame) in the form of relativistic particles, in units of 10^{43} erg s $^{-1}$, as used for our modelling. The dashed lines represent the relationships predicted by the Katarzyński & Ghisellini (2007) model. The labelled dates identify the specific model/state of the source (see Table 3). *Bottom panel:* The power carried by the jet in the form of magnetic field (L_B), cold protons (L_p), relativistic electrons (L_e) resulting from our modelling, as a function of the bulk Lorentz factor.

TABLE 1
Swift/XRT OBSERVATION LOG^a

Start time (UT) (yyyy-mm-dd hh:mm:ss)	End time (UT) (yyyy-mm-dd hh:mm:ss)	Exposure (s)	Mean Flux ^b (0.5–10 keV)	Counts (0.2–10 keV)	Spectral index	χ^2_{red} (d.o.f.) C-stat (%)
2004-12-23 23:37:34	2004-12-23 23:59:40	1029	$0.67^{+0.83}_{-0.50}$	168	0.75 ± 0.18	372.7 (32.2) ^c
2005-01-27 00:05:19	2005-01-27 22:37:41	7248	$1.49^{+0.10}_{-0.08}$	2660	0.73 ± 0.05	1.06 (101)
2005-01-28 00:08:16	2005-01-28 23:03:41	22663	1.38 ± 0.05	7794	0.76 ± 0.03	1.12 (244)
2005-02-24 16:19:51	2005-02-25 12:00:40	18592	1.26 ± 0.05	5420	0.65 ± 0.03	0.99 (198)
2005-07-12 01:13:01	2005-07-12 11:12:59	4977	1.05 ± 0.11	1003	0.57 ± 0.07	0.93 (44)
2005-11-17 00:45:12	2005-11-17 12:11:11	6373	0.39 ± 0.06	556	$0.75^{+0.11}_{-0.10}$	1.16 (23)
2005-11-24 22:14:00	2005-11-25 11:25:57	6243	$0.44^{+0.07}_{-0.06}$	583	0.77 ± 0.10	1.00 (24)

^aAll observations were carried out with XRT in PC observing mode.

^bUnabsorbed flux in units of 10^{-11} erg cm⁻² s⁻¹. The effects of PSF-loss and vignetting were taken into account in the count rate to flux conversion.

^cCash statistic (C-stat) and percentage of Monte Carlo realizations that had statistic < C-stat, for this entry only.

TABLE 2
Swift/UVOT AND REM OBSERVATIONS OF PKS 0537-441 IN JULY AND NOVEMBER 2005^a

Date (UT)	MJD ^b	magnitude ^c
UVOT UVW2 filter (1930 Å)		
2005 Nov 24.9243	53698.9243	17.02 ± 0.04^d
24.9958	53698.9958	16.86 ± 0.04
25.0646	53699.0646	17.00 ± 0.05
25.2042	53699.2042	16.91 ± 0.07
25.3313	53699.3313	16.95 ± 0.05
25.3979	53699.3979	17.03 ± 0.05
25.4653	53699.4653	16.98 ± 0.05
UVOT UVM2 filter (2200 Å)		
2005 Nov 24.9312	53698.9312	16.77 ± 0.05
25.0007	53699.0007	16.88 ± 0.06
25.0688	53699.0688	16.64 ± 0.06
25.1382	53699.1382	16.60 ± 0.08
25.2063	53699.2063	16.59 ± 0.09
25.3361	53699.3361	16.89 ± 0.07
25.4028	53699.4028	16.76 ± 0.06
25.4701	53699.4701	16.73 ± 0.06
UVOT UVW1 filter (2600 Å)		
2005 Nov 24.9354	53698.9354	16.60 ± 0.05
25.0035	53699.0035	16.53 ± 0.06
25.0715	53699.0715	16.70 ± 0.07
25.1396	53699.1396	16.66 ± 0.10
25.2076	53699.2076	16.62 ± 0.10
25.3389	53699.3389	16.40 ± 0.06
25.4056	53699.4056	16.67 ± 0.06
25.4729	53699.4729	16.51 ± 0.06
UVOT U filter (3450 Å)		
2005 Jul 12.0530	53563.0530	14.05 ± 0.16
12.1190	53563.1190	14.03 ± 0.16
Nov 17.0368	53691.0368	16.22 ± 0.03
17.1042	53691.1042	16.27 ± 0.03
17.1736	53691.1736	16.24 ± 0.05
17.2201	53691.2201	16.33 ± 0.06

TABLE 2—*Continued*

Date (UT)	MJD ^b	magnitude ^c
17.2424	53691.2424	16.16 ± 0.16
17.2896	53691.2896	16.15 ± 0.03
17.3590	53691.3590	16.16 ± 0.03
17.4264	53691.4264	16.19 ± 0.02
17.4986	53691.4986	16.22 ± 0.02
24.9375	53698.9375	16.49 ± 0.05
25.0056	53699.0056	16.56 ± 0.06
25.0736	53699.0736	16.37 ± 0.06
25.1409	53699.1409	16.50 ± 0.09
25.2083	53699.2083	16.62 ± 0.10
25.3409	53699.3409	16.57 ± 0.06
25.4076	53699.4076	16.60 ± 0.06
25.4743	53699.4743	16.63 ± 0.06
UVOT B filter (4350 Å)		
2005 Jul 12.0560	53563.0560	14.81 ± 0.08
12.1220	53563.1220	14.76 ± 0.08
Nov 17.0403	53691.0403	16.97 ± 0.03
17.1076	53691.1076	16.99 ± 0.04
17.1750	53691.1750	17.03 ± 0.07
17.2208	53691.2208	17.00 ± 0.07
17.2917	53691.2917	17.03 ± 0.04
17.3625	53691.3625	16.99 ± 0.03
17.4306	53691.4306	16.97 ± 0.03
17.5056	53691.5056	16.97 ± 0.02
24.9389	53698.9389	17.36 ± 0.06
25.0069	53699.0069	17.31 ± 0.08
25.0743	53699.0743	17.37 ± 0.10
25.1409	53699.1409	17.25 ± 0.14
25.3417	53699.3417	17.34 ± 0.08
25.4090	53699.4090	17.31 ± 0.08
25.4757	53699.4757	17.22 ± 0.08
UVOT V filter (5460 Å)		
2005 Jul 12.0500	53563.0500	14.32 ± 0.09
12.1150	53563.1150	14.25 ± 0.09
Nov 17.0340	53691.0340	16.47 ± 0.04
17.1014	53691.1014	16.39 ± 0.04
17.1729	53691.1729	16.46 ± 0.07

TABLE 2—*Continued*

Date (UT)	MJD ^b	magnitude ^c
17.2194	53691.2194	16.58 ± 0.15
17.2424	53691.2424	16.36 ± 0.21
17.2875	53691.2875	16.48 ± 0.05
17.3556	53691.3556	16.44 ± 0.04
17.4222	53691.4222	16.43 ± 0.04
17.4910	53691.4910	16.42 ± 0.03
24.9286	53698.9286	16.81 ± 0.04
25.0000	53699.0000	16.82 ± 0.09
25.0681	53699.0681	16.88 ± 0.10
25.1382	53699.1382	16.72 ± 0.13
25.2055	53699.2055	16.85 ± 0.15
25.3354	53699.3354	16.84 ± 0.10
25.4021	53699.4021	16.89 ± 0.10
25.4694	53699.4694	17.02 ± 0.11
REM V filter (5505 Å)		
2005 Jul 07.4375	53558.4375	15.72 ± 0.03
09.4219	53560.4219	15.21 ± 0.02
10.4336	53561.4336	14.80 ± 0.02
11.4297	53562.4297	14.40 ± 0.02
12.4297	53563.4297	14.52 ± 0.02
12.4375	53563.4375	14.47 ± 0.02
12.4414	53563.4414	14.50 ± 0.02
22.3984	53573.3984	15.47 ± 0.04
22.4336	53573.4336	15.73 ± 0.03
Nov 07.2494	53681.2494	16.93 ± 0.11
19.2346	53693.2346	17.07 ± 0.13
20.2174	53694.2174	17.17 ± 0.14
30.2021	53704.2021	17.46 ± 0.17
REM R filter (6588 Å)		
2005 Jul 07.4375	53558.4375	15.06 ± 0.01
09.4219	53560.4219	14.56 ± 0.01
11.4336	53562.4336	13.75 ± 0.04
12.4258	53563.4258	13.91 ± 0.01
12.4297	53563.4297	13.91 ± 0.01
12.4375	53563.4375	13.87 ± 0.01
13.4414	53564.4414	14.04 ± 0.06
22.4023	53573.4023	14.87 ± 0.02

TABLE 2—*Continued*

Date (UT)	MJD ^b	magnitude ^c
Nov 06.2533	53680.2533	16.39 ± 0.07
07.2522	53681.2522	16.39 ± 0.04
18.2249	53692.2249	16.41 ± 0.06
19.2452	53693.2452	16.20 ± 0.06
20.2280	53694.2280	16.35 ± 0.07
30.2127	53704.2127	16.92 ± 0.08
REM I filter (8060 Å)		
2005 Jul 07.4375	53558.4375	14.40 ± 0.01
09.4219	53560.4219	13.91 ± 0.01
10.4375	53561.4375	13.48 ± 0.01
11.4336	53562.4336	13.14 ± 0.03
12.4258	53563.4258	13.26 ± 0.01
12.4336	53563.4336	13.23 ± 0.01
12.4414	53563.4414	13.24 ± 0.01
20.4414	53571.4414	13.82 ± 0.03
22.4062	53573.4062	14.13 ± 0.02
22.4375	53573.4375	14.22 ± 0.02
Nov 06.2559	53680.2559	15.60 ± 0.08
07.2549	53681.2549	15.78 ± 0.07
18.2355	53692.2355	15.82 ± 0.08
19.2560	53693.2560	15.72 ± 0.07
20.2386	53694.2386	15.89 ± 0.10
30.2235	53704.2235	16.23 ± 0.09
REM H filter (16000 Å)		
2005 Nov 02.1718	53676.1718	12.77 ± 0.07
02.1738	53676.1738	12.89 ± 0.08
02.1759	53676.1759	12.93 ± 0.08
02.1805	53676.1805	12.89 ± 0.10
02.1820	53676.1820	12.70 ± 0.06
02.1917	53676.1917	12.80 ± 0.07
02.1941	53676.1941	12.75 ± 0.07
02.1962	53676.1962	12.85 ± 0.07
02.2003	53676.2003	12.77 ± 0.08
02.2895	53676.2895	12.75 ± 0.07
02.2957	53676.2957	13.05 ± 0.06
02.3027	53676.3027	12.88 ± 0.08
02.3048	53676.3048	12.78 ± 0.07

TABLE 2—*Continued*

Date (UT)	MJD ^b	magnitude ^c
02.3068	53676.3068	12.73 ± 0.06
02.3089	53676.3089	12.96 ± 0.08
03.2822	53677.2822	12.95 ± 0.07
03.2864	53677.2864	12.78 ± 0.06
03.2885	53677.2885	12.83 ± 0.07
03.2905	53677.2905	12.72 ± 0.06
03.2929	53677.2929	12.66 ± 0.06
03.2950	53677.2950	12.91 ± 0.09
03.3006	53677.3006	12.78 ± 0.07
03.3027	53677.3027	12.70 ± 0.08
03.3047	53677.3047	12.63 ± 0.07
03.3068	53677.3068	12.80 ± 0.07
03.3088	53677.3088	12.67 ± 0.06
03.3112	53677.3112	12.90 ± 0.08
03.3133	53677.3133	12.98 ± 0.07
03.3154	53677.3154	12.84 ± 0.07
03.3174	53677.3174	12.98 ± 0.07
03.3195	53677.3195	12.95 ± 0.07
03.3219	53677.3219	13.08 ± 0.07
03.3240	53677.3240	12.75 ± 0.07
03.3260	53677.3260	12.79 ± 0.06
03.3281	53677.3281	12.74 ± 0.06
03.3302	53677.3302	12.84 ± 0.08
17.1083	53691.1083	12.42 ± 0.08
18.2154	53692.2154	12.68 ± 0.06
18.2208	53692.2208	12.64 ± 0.07
18.2229	53692.2229	12.61 ± 0.08
18.2249	53692.2249	12.70 ± 0.07
2005 Nov 18.2273	53692.2273	12.64 ± 0.06
18.2296	53692.2296	12.63 ± 0.07
18.2314	53692.2314	12.74 ± 0.06
18.2335	53692.2335	12.73 ± 0.07
18.2355	53692.2355	12.61 ± 0.06
18.2379	53692.2379	12.71 ± 0.07
18.2399	53692.2399	12.51 ± 0.06
18.2420	53692.2420	12.61 ± 0.07
18.2440	53692.2440	12.70 ± 0.06
18.2461	53692.2461	12.60 ± 0.07
18.2626	53692.2626	12.68 ± 0.07
18.2654	53692.2654	12.68 ± 0.07
18.2688	53692.2688	12.62 ± 0.07

TABLE 2—*Continued*

Date (UT)	MJD ^b	magnitude ^c
19.2350	53693.2350	12.65 ± 0.07
19.2371	53693.2371	12.54 ± 0.08
19.2391	53693.2391	12.72 ± 0.08
19.2412	53693.2412	12.65 ± 0.08
19.2432	53693.2432	12.55 ± 0.07
19.2453	53693.2453	12.59 ± 0.07
19.2476	53693.2476	12.52 ± 0.07
19.2497	53693.2497	12.54 ± 0.08
19.2518	53693.2518	12.66 ± 0.07
19.2605	53693.2605	12.54 ± 0.06
20.2220	53694.2220	12.74 ± 0.07
20.2240	53694.2240	12.96 ± 0.07
20.2249	53694.2249	12.66 ± 0.06
20.2261	53694.2261	12.83 ± 0.07
20.2281	53694.2281	12.83 ± 0.06
20.2346	53694.2346	12.77 ± 0.06
20.2366	53694.2366	12.62 ± 0.05
20.2387	53694.2387	12.76 ± 0.06
20.2411	53694.2411	12.74 ± 0.06
20.2431	53694.2431	12.85 ± 0.07
20.2452	53694.2452	12.77 ± 0.07
20.2472	53694.2472	12.82 ± 0.07
20.2493	53694.2493	12.66 ± 0.06
20.2513	53694.2513	12.74 ± 0.07
30.1977	53704.1977	13.10 ± 0.08
30.2115	53704.2115	13.20 ± 0.10
30.2135	53704.2135	13.33 ± 0.11
30.2179	53704.2179	13.37 ± 0.10
30.2200	53704.2200	13.08 ± 0.10
30.2371	53704.2371	13.20 ± 0.10

^aTypical exposure times are 4-5 minutes, both for UVOT and REM.

^bModified Julian Date. We used the convention $\text{MJD} = \text{JD} - 2,400,000.5$.

^cNot corrected for Galactic extinction.

^dErrors represent 1 σ statistical uncertainties.

TABLE 3
MODEL PARAMETERS

Feb 05	Jul 05	Nov 05	1991–1992	1995	Units	
Γ	10	12	15	15	15	
R	16	19	28	28	28	[10^{15} cm]
B	40	12	7	6	7	[G]
γ_b	250	500	380	200	310	
γ_{\max}	3e3	6e3	2e4	7e3	2e4	
p	3.8	4.4	6.2	3.5	4.2	
L'_{inj}	0.095	0.07	0.025	0.045	0.03	[10^{45} erg s $^{-1}$]
ν_{ext}	0.3	0.5	1.5	1.5	1.5	[10^{15} Hz]
U_{ext}	0.085	0.069	0.016	0.016	0.016	[erg cm $^{-3}$]
δ	15.7	17.2	18.6	18.6	18.6	
L_B	253	28	32.3	23.8	32.3	[10^{45} erg s $^{-1}$]
L_p	24.5	42	53.2	96.8	46.6	[10^{45} erg s $^{-1}$]
L_e	0.08	0.18	0.29	0.51	0.25	[10^{45} erg s $^{-1}$]
L_{rad}	8.8	10.2	5.6	9.95	5.5	[10^{45} erg s $^{-1}$]

NOTE.—For all models we have assumed a viewing angle $\theta = 3^\circ$ and a bolometric luminosity of the accretion disk $L_{\text{disk}} = 1.8 \times 10^{46}$ erg s $^{-1}$. The energy density of the external radiation and its peak frequency ν_{ext} are measured in the observer frame.